International Journal of Thermal Sciences 49 (2010) 1799–1812

Contents lists available at ScienceDirect

International Journal of Thermal Sciences

journal homepage: www.elsevier.com/locate/ijts

Hydrodynamic-thermal boundary layer development and mass transfer characteristics of a circular cylinder in confined flow

A. Alper Ozalp [a,*], Ibrahim Dincer [b,1]

[a] Department of Mechanical Engineering, University of Uludag, 16059 Gorukle, Bursa, Turkey
[b] Faculty of Engineering and Applied Science, University of Ontario Institute of Technology, 2000 Simcoe Street North, Oshawa, Ontario L1H 7K4, Canada

ARTICLE INFO

Article history:
Received 19 July 2009
Received in revised form
19 March 2010
Accepted 22 April 2010
Available online 2 June 2010

Keywords:
Blockage
Boundary layer
Separation
Wall shear
Heat transfer
Mass transfer

ABSTRACT

The effects of blockage on the hydrodynamic, thermal and mass transfer characteristics of a circular cylinder (CC) and their association with each other are investigated numerically, by considering the influence of blockage ($\beta = 0.333-0.800$) on the flow and heat transfer mechanisms in conjunction with moisture diffusivity ($D = 1 \times 10^{-8}-1 \times 10^{-5}$ m^2/s) to show how much mass transfer behavior and phenomena are affected. As some comprehensive ANSYS-CFX runs are performed in the hydrodynamic and thermal fields around the CC, the moisture distributions within the CC are evaluated by Alternating Direction Implicit method. It is determined that blockage causes thinner hydrodynamic and thermal boundary layers, rises the frictional and thermal activities, and shifts the separation locations (θ_s) downstream to $\theta_s = 50.20^\circ$, 41.98° and 37.30° for $\beta = 0.333$, 0.571 and 0.800. In the complete blockage scenario set, stagnation point heat transfer values are evaluated to be above those of the back-face, signifying the superior heat transfer enhancing capability of the stagnation point momentum activity when compared with the impact of downstream vortex system. The influence of moisture diffusivity on the overall drying times is determined to advance with stronger blockage. As the back face mass transfer coefficients ($h_{m\text{-}bf}$) rise with a high β, the contrary is valid for front face values ($h_{m\text{-}ff}$), with the interpreting ratios of $\overline{h}_{m\text{-}bf}/\overline{h}_m = 0.51$ and 0.57 and $\overline{h}_{m\text{-}ff}/\overline{h}_m = 1.49$ and 1.43 for $\beta = 0.333$ and 0.800.

1. Introduction

Circular cylinder (CC), being one of the major structural configurations utilized in various branches of industry, is mostly recognized by the heat and mass transfer characteristics, especially when exposed to fluid flow. As CCs are employed in a wide range of applications, such as crystal growth processes and furnace design [1], oceanography and electric conductors [2], material science [3] and drying applications [4], the formation of thermal and hydrodynamic boundary layers around the solid boundary is critically important to provide optimum processing conditions and product quality. In this regard, the heat and mass aspects of the process gain outmost importance from the point of achieving the optimum output to accomplish the industrial requirement. In certain specific practices and equipments, CCs are subjected to confined flows, or flows with blockage, which can give rise to exceptional characteristics not only in the flow field around the CC, but also in the heat transfer to/from/in the CC, which jointly structure the mass transfer mechanisms as well. Due to these scientific fundamentals and necessities, a research study, concentrating on the flow, heat and mass transfer characteristics of a CC in confined flow, must encompass the 3 main concerns: (i) boundary layer development and flow characteristics, (ii) heat transfer mechanism and (iii) mass transfer behavior.

As industrial applications, involving confined flows, are becoming more common, the research need on the boundary layer development has become more apparent as one of new research fields on flows with blockage around not only CCs [5–9] but also square cylinders (SC) [10,11]. As friction and total drag coefficients on the CC, in the blockage ratio range of $\beta = 0.05-0.65$, were studied by Chakraborty et al. [5], wake behavior, vortex shedding, re-circulation and separation lengths of the CC, for the blockage range of $\beta = 0.05-0.9$, were taken into consideration by Griffith et al. [6]. Sen et al. [7] performed steady numerical computations in the Reynolds number and blockage ratio ranges of $Re_d = 6-40$ and $\beta = 0-0.8$ and investigated the variation of bubble length, separation angle and drag force characteristics. For the blockage case of $\beta = 0.333$ steady and unsteady regime investigations, within the Reynolds number range of $Re_d = 30-277$, were carried out by Rehimi et al. [8]. They stated that for $Re_d < 108$, the streamlines and the pathlines are confounded characteristics of a steady regime and

* Corresponding author. Tel./fax: +90 224 442 8899.
E-mail addresses: aozalp@uludag.edu.tr (A. Alper Ozalp), ibrahim.dincer@uoit.ca (I. Dincer).
[1] Tel.: +1 905 721 8668.

1290-0729/$ – see front matter © 2010 Elsevier Masson SAS. All rights reserved.
doi:10.1016/j.ijthermalsci.2010.04.016

Nomenclature

C_f	friction coefficient
C_p	pressure coefficient
C_p	constant pressure specific heat, J kg^{-1} K^{-1}
d	diameter, m
D	moisture diffusivity, m^2 s^{-1}
h	convective heat transfer coefficient, W m^{-2} K^{-1}
h_m	mass transfer coefficient, m s^{-1}
H	duct height, m
k	thermal conductivity, W m^{-1} K^{-1}
Le	Lewis number
L_r	recirculation length, m
M	moisture content, kg kg^{-1}
Nu	Nusselt number
P	static pressure, Pa
Re_d	Reynolds number
t	time, s
T	temperature, K
u	velocity in x-direction, m s^{-1}
U_∞	average velocity of air at the inlet, m s^{-1}
v	velocity in y-direction, m s^{-1}
w	width, mm
x	coordinate in x-direction, m
y	coordinate in y-direction, m

Greek symbols

α	thermal diffusivity, m^2 s^{-1}
β	blockage ratio
ϕ	dimensionless moisture
λ	under-relaxation parameter
μ	dynamic viscosity, Pa s
θ	angular position, Deg
ρ	density, kg m^{-3}
τ_w	wall shear stress, Pa
ζ	dimensionless temperature

Subscripts

a	air, average
bf	back-face
c	center
cyl	cylinder
ds	downstream
ff	front-face
i	initial
od	overall drying
max	maximum
n	normal to the cylinder surface
θ	angular
rev	reverse
s	separation, cylinder surface
th	throat
tm	thermal mixing
T	temperature
us	upstream
∞	inlet air

Superscript

_	average

the flow is characterized by two fixed counter-rotating vortices downstream of the cylinder. In a similar work, Sahin and Owens [9] performed computations for the Reynolds number and blockage ratio ranges of $Re_d = 0–280$ and $\beta = 0.1–0.9$ and reported the neutral stability limit as $Re \approx 100$ for $\beta = 0.333–0.800$. From SC point of view, Camarri and Giannetti [10] worked on the role of blockage ($\beta = 0.1–0.17$) on unsteady wake interaction between the wake and the flow close to the confining walls; Breuer et al. [11] discussed steady and unsteady flows through re-circulation lengths and drag coefficients for the blockage ratio of $\beta = 0–0.800$.

The available literature on the heat transfer issues of CCs considered the effects of fluid properties and the characteristic non-dimensional numbers on the local and mean heat transfer values. The effects of Re and Pr on average and local Nu distributions during forced convection heat transfer to incompressible Newtonian and non-Newtonian fluids from a heated circular cylinder in the steady cross-flow regime was numerically studied by Bharti et al. [12]. Chang and Mills [13] experimentally evaluated enhanced, circumferentially averaged and total averaged Nusselt numbers with different aspect ratios. Khan et al. [14] developed closed form drag and average heat transfer coefficient expressions for wide ranges of Re and Pr numbers by applying the integral approach to the boundary layer analysis.

The variation of heat transfer characteristics of cylinders in the presence of blockage effects has attracted attention of some researchers only. Local static pressure and Nu number variations on the cylinder surface and also the isotherm and streamline contours in the wake region of the CC, placed in laminar flow with the blockage ratio range of $\beta = 0.17–0.48$, were numerically studied by Buyruk et al. [15]. Fluid flow around and heat transfer from a CC between parallel planes for $\beta = 0.10–0.90$ were investigated numerically through an integral approach by Khan et al. [16], who reported that blockage ratio not only delays the separation but also characterizes the fluid flow around and the heat transfer from the cylinder. The related literature also offers a few studies reporting the laminar heat transfer mechanism of SCs, placed in confined flow. Both Dhiman et al. [17] and Sharma and Eswaran [18] presented their fluid flow findings in terms of velocity profiles, friction and drag coefficients and discussed wake generation for different β ranges ($\beta = 0.125–0.25$ [17], $\beta = 0.1–0.5$ [18]). Additionally, they detailed their heat transfer evaluations through cross debates and associations with the fluid flow analysis.

From the point of either to concentrate on a particular application frame or to propose an applicable theory, the drying kinetics and the mass transfer mechanism of moist objects have been the focus of several researches. Queiroz and Nebra [19] investigated the effects of surface convective mass transfer of bananas by treating the experimental data of moisture content during drying through a diffusion model, and reported theoretical and experimental drying kinetics results under different air drying conditions. Akpinar and Dincer [20] at the first step experimentally determined the drying times of potato pieces and in the second step applied numerical drying models to evaluate moisture content distributions, moisture transfer parameters and the drying process parameters. The unsteady effects of material parameters such as Prandtl number, Schmidt number and buoyancy ratio parameter on the velocity, temperature and concentration are investigated by Ganesan and Rani [21], who determined that mass transfer rate is enhanced with higher Schmidt number. Kaya et al. [22] numerically modeled the forced convection drying of moist objects and predicted that the convective heat and mass transfer coefficients in the left half of the cylindrical object are higher than those in the right half. Heat and moisture transfer during drying of a cylindrical object were computationally analyzed by Hussain and Dincer [23].

They determined that although the moisture gradient became almost steady as drying progresses, considerably higher gradients were recorded in the early drying period. Kondjoyan [24] reviewed, mainly for the solids of more complex shapes, the heat and mass transfer coefficients of air chilling and storage of solid food products. As Dincer et al. [25] developed and verified new drying correlations to determine the moisture transfer parameters, such as, moisture diffusivity and moisture transfer coefficients, a graphical method, to estimate the moisture transfer parameters and drying times in a quick and efficient manner, was proposed by Sahin and Dincer [26]. Panagiotou et al. [27] retrieved and analyzed a wide collection of moisture diffusivity values, for various foods, from the recent publications. They also classified the data of more than 100 food materials in 11 categories. Double-diffusive laminar mixed convection was numerically considered by Teamah [28], who determined that mass diffusion becomes stronger with the increase of Lewis number. McMinn and Magee [29] investigated the moisture transport in potato cylinders by considering the effects of air velocity and temperature on the drying rate.

Although the heat transfer characteristics are significantly dependent on the fluid flow and boundary layer development, and the mass transfer coefficients are determined by those of the heat transfer, in spite of the several existing CC studies, the available related literature is incapable of responding to a demand on the association of hydrodynamic boundary layer development and mass transfer of CCs in confined flows. The purposes of the present work are (i) to identify the effects of blockage on the boundary layer development, heat transfer rates and mass transfer behavior of CCs, (ii) to outline in detail the mechanisms of the interrelation among the boundary layer development, heat transfer characteristics and mass transfer schemes of CCs. Issues on the fluid flow and boundary layer development are investigated in terms of streamlines, velocity profiles, separation phenomena, surface static pressures and wall shear stresses. Further studies on heat transfer are carried out through temperature profiles/contours and convective heat transfer coefficients. The mass transfer characteristics are presented by mass transfer coefficients, overall drying times, local drying schemes and iso-moisture contours inside the CC. The entire analysis and reporting are built up on wide ranges of blockage ratios and moisture diffusivities.

2. Modeling and solution methodologies

2.1. Fundamental equations

The geometry and the corresponding dimensions considered in the analysis are presented in Fig. 1. To structure the flow domain in accord with the aim of the work, blockage scenario is implemented by placing two adiabatic channel walls on either side of the cylinder, having a distance of H/2 to the centerline. As a fully-developed laminar velocity profile of $u(y) = \frac{3}{2}U_\infty[1-(\frac{2y}{H})^2]$ is employed for air at the duct inlet (Fig. 1(a)), U_∞ being the average velocity, the inlet temperature is characterized by T_∞. To construct and carry out the fluid flow and heat-mass transfer investigations in a common systematic convention, the angular coordinate system and the surface points of S_1 ($\theta = 0^\circ$), S_2 ($\theta = 180^\circ$) and S_3 ($\theta = 90^\circ$) are identified (Fig. 1(b)) on the two-dimensional circular cylinder, whose diameter and fixed temperature are defined by d and T_s respectively.

Fluid flows around CCs are approved to be laminar up to the Reynolds number of $Re_d \leq 2\times10^5$ by the fundamental fluid mechanics theory [30]. Recently Rehimi et al. [8] and Sahin and Owens [9] investigated the confined flows around CCs. As the critical Reynolds number for wake instability and appearance of the von Karman vortices was reported as $Re_d = 108$ in [8], the neutral stability limit for the blockage range of $\beta = 0.333$–0.800 was evaluated as $Re_d \approx 100$ in [9]. In the present study, computational analysis are carried out at the constant Reynolds number of $Re_d = 40$, which is sufficiently below the critical Reynolds number and scientifically appropriate for laminar boundary layer development on the CC surface. On the other hand, from the point of channel flow the blockage ratio ($\beta = d/H$) range of $\beta = 0.333 \rightarrow 0.800$ is characterized in the analyses by varying the duct height (H) with the appropriate values of $H = 120 \rightarrow 50$ mm

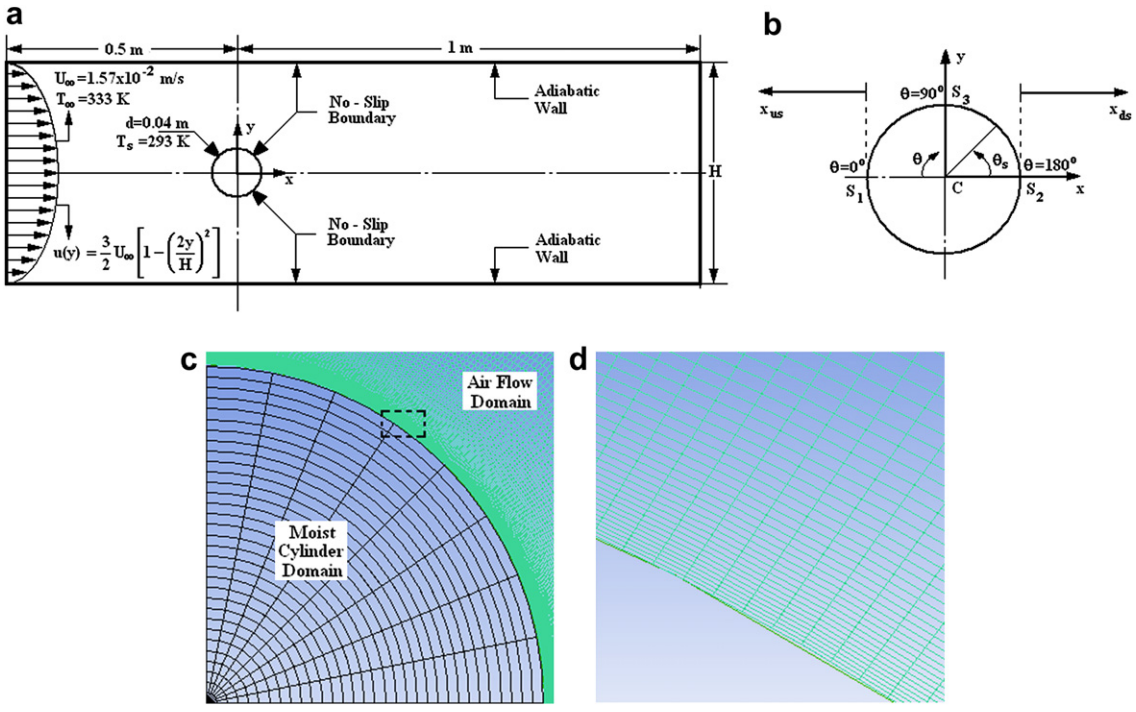

Fig. 1. (a) Flow domain around the cylinder, (b) the coordinate system, the grid resolution (c) in and (d) around the cylinder interface.

(Fig. 1(a)). The corresponding Reynolds number range for the channel flow arises as Re = 240 → 100, which are as well below the traditional critical Reynolds number of Re = 2300 [30]. Being compatible with these definitions, steady ($\partial/\partial t = 0$), incompressible and constant thermal property laminar fluid flow and heat transfer analysis are handled in the master Cartesian coordinate system with the following two-dimensional continuity, momentum and energy equations.

Continuity:

$$\frac{\partial u}{\partial x}+\frac{\partial v}{\partial y}=0 \tag{1}$$

Momentum:

$$\rho\left(u\frac{\partial u}{\partial x}+v\frac{\partial u}{\partial y}\right)=-\frac{\partial P}{\partial x}+\mu\left(\frac{\partial^2 u}{\partial x^2}+\frac{\partial^2 u}{\partial y^2}\right) \tag{2a}$$

$$\rho\left(u\frac{\partial v}{\partial x}+v\frac{\partial v}{\partial y}\right)=-\frac{\partial P}{\partial y}+\mu\left(\frac{\partial^2 v}{\partial x^2}+\frac{\partial^2 v}{\partial y^2}\right) \tag{2b}$$

Energy:

$$u\frac{\partial T}{\partial x}+v\frac{\partial T}{\partial y}=\alpha\left(\frac{\partial^2 T}{\partial x^2}+\frac{\partial^2 T}{\partial y^2}\right) \tag{3}$$

Since one of the aims of the present work is to inspect the drying characteristics of the CC, the analogous analysis must be capable of evaluating the variation of moisture levels both in time and inside the CC. Thus, in spite of the steady behavior of the hydrodynamic and thermal characteristics around the CC, the decaying mechanism of the moisture within the CC, due to the forced convection driven drying activity, must also be enlightened. Due to these scientific requirements, and with the assumption that shrinkage or deformation of the material during drying is negligible, the interior mass transfer mechanism of the dried object is characterized by the two-dimensional moisture transfer equation of Eq. (4).

$$\frac{1}{D}\frac{\partial M}{\partial t}=\frac{1}{r}\frac{\partial M}{\partial r}+\frac{\partial^2 M}{\partial r^2}+\frac{1}{r^2}\frac{\partial^2 M}{\partial \theta^2} \tag{4}$$

2.2. Boundary conditions

As a fully developed duct flow velocity profile is employed at the channel inlet, channel walls and the cylinder surface are assigned with no-slip boundary condition ($u = v = 0$). The flow enters the channel with the free-stream temperature of T_∞, interacts both hydrodynamically and thermally with the constant temperature (T_s) CC; however experiences no heat transfer with the channel walls (adiabatic) and leaves the channel with atmospheric pressure. As the original moisture content inside the CC is expressed by the initial condition of Eq. (5a), the angular boundary conditions are both located at $\theta = 0 = 2\pi$ (Eqs. (5b) and (5c)), and those of the radial appear at the center (Eq. (5d)) and on the surface (Eq. (5e)) of the drying object.

$$M(r,\theta,0)=M_i \tag{5a}$$

$$M(r,0,t)=M(r,2\pi,t) \tag{5b}$$

$$\frac{\partial M(r,0,t)}{\partial \theta}=\frac{\partial M(r,2\pi,t)}{\partial \theta} \tag{5c}$$

$$\frac{\partial M(0,\theta,t)}{\partial r}=0 \quad \text{at } r=0 \tag{5d}$$

$$-D\frac{\partial M(R,\theta,t)}{\partial r}=h_m(M-M_a) \quad \text{at } r=R \tag{5e}$$

2.3. Flow, heat and mass transfer parameters

The following key parameters are employed in the modeling study, to fit the present computational outputs, and the consequently stemming discussions, not only with the formation style but also with the commenting strategy of the available related literature.

$$\beta=\frac{d}{H} \quad \mathrm{Re}_d=\frac{\rho U_\infty d}{\mu} \quad C_p=\frac{P_\theta-P_\infty}{1/2\rho U_\infty^2}$$

$$\tau_w=C_f 1/2\rho U_\infty^2 \quad -k\frac{\partial T}{\partial n}\Big|_s=h_\theta(T_s-T_a) \tag{6a–e}$$

$$\mathrm{Nu}_\theta=\frac{h_\theta d}{k} \quad \mathrm{Nu}_{ave}=\frac{1}{2\pi}\int_0^{2\pi}\mathrm{Nu}_\theta d\theta \quad \zeta=\frac{T-T_s}{T_\infty-T_s}$$

$$h_m=h_\theta\left(\frac{D\mathrm{Le}^{1/3}}{k}\right) \quad \phi=\frac{M-M_a}{M_i-M_a} \tag{6f–j}$$

where β is the blockage ratio, $\mathrm{Re_d}$ is the Reynolds number, C_p is the pressure coefficient, τ_w is the wall shear stress, h_θ is the local convective heat transfer coefficient, Nu_θ and $\mathrm{Nu_{ave}}$ are the local and average Nusselt numbers, ζ is the dimensionless temperature, h_m is the mass transfer coefficient defined by the Lewis analogy [30], ϕ is the dimensionless moisture content.

2.4. Methodological strategy

Air flow domain (Fig. 1(a) and (c)), bounded by the channel walls and the CC, and the internal region of the moist cylinder (Fig. 1(c)) are methodologically handled by two independent computational strategies. ANSYS-CFX [31], structured on the element-based finite-volume method, is employed for the constant thermal property computations of the fluid flow and heat transfer mechanisms, where the multigrid solver is scalably adopted to the flow domain. For the diffusion simulations inside the moist cylinder, the Alternating Direction Implicit Method is used.

In the flow and heat transfer analyses, to enhance the computational capabilities on predicting the velocity and temperature gradients in the complete blockage range considered, refined mesh size is employed in the neighborhood of the solid boundaries with the expansion factor of 1.1 (Fig. 1(d)). For each blockage case, several tests are conducted not only to decide on the optimum grid nodes but also to ensure that the results presented here are independent of the meshing strategy. Table 1 displays a summary of these tests for the 3 blockage cases of $\beta = 0.333$, 0.571 and 0.800 in terms of the fluid flow and heat transfer parameters that are the primary concerns of the present research. To act in conjunction with the meshing strategies, a considerably sensitive convergence criterion of 1×10^{-7} is used for all parameters in the continuity, momentum and energy equations (Eqs. (1)–(3)).

For the mass transfer computations within the CC, the two-dimensional moisture transfer equation of Eq. (4) is splitted into two finite difference equations: the first with the r-derivative (Eq. (7a)) and the second with the θ-derivative (Eq. (7b)). An implicit action is taken in either of the directions with the Alternating

Table 1
Grid node effects on fluid flow and heat transfer parameters (*: Optimum Grid Nodes).

β	# of Nodes	$(P_s)_{\theta=0}$ (Pa)	$(\tau_w)_{max}$ (Pa)	Nu_{ave}
0.333	337216	0.00081	0.00019	4.172
	408358	0.00084	0.00019	4.082
	423137	0.00086	0.00020	4.055
	431216*	0.00086	0.00020	4.051
0.571	293517	0.00220	0.00032	5.140
	354713	0.00231	0.00036	5.019
	364872	0.00233	0.00036	4.977
	374723*	0.00234	0.00037	4.968
0.800	287437	0.01293	0.00165	6.730
	346831	0.01321	0.00177	6.547
	358195	0.01329	0.00182	6.521
	367048*	0.01332	0.00184	6.513

Direction Implicit (ADI) method, which is a finite difference method for solving parabolic and elliptic partial differential equations in two or more dimensions. Since mass transfer coefficient (h_m) is dependent on the convective heat transfer coefficient (h_θ – Eq. (6i)), ANSYS-CFX outputs the h_θ variation on the cylinder surface and as well generates the h_m distribution. The initial and boundary conditions (Eq. (5)) of the mass transfer mechanism are as well integrated in the solution logic of Eq. (7). The mass transfer analyses are performed with the optimum mesh density of 31×31 (Fig. 1 (c)), beyond which the local and time dependent moisture values changed insensibly.

$$M_{i,j}^{n+1}\left(\frac{2}{D\Delta t}+\frac{2}{\Delta r^2}\right)-M_{i+1,j}^{n+1}\left(\frac{1}{2r\Delta r}+\frac{1}{\Delta r^2}\right)+M_{i-1,j}^{n+1}\left(\frac{1}{2r\Delta r}-\frac{1}{\Delta r^2}\right)=M_{i,j}^{n+1/2}\left(\frac{2}{D\Delta t}-\frac{2}{r^2\Delta\theta^2}\right)+M_{i,j+1}^{n+1/2}\left(\frac{1}{r^2\Delta\theta^2}\right)+M_{i,j-1}^{n+1/2}\left(\frac{1}{r^2\Delta\theta^2}\right) \tag{7a}$$

$$M_{i,j}^{n+1/2}\left(\frac{2}{D\Delta t}+\frac{2}{r^2\Delta\theta^2}\right)-M_{i,j+1}^{n+1/2}\left(\frac{1}{r^2\Delta\theta^2}\right)-M_{i,j-1}^{n+1/2}\left(\frac{1}{r^2\Delta\theta^2}\right)=M_{i,j}^{n}\left(\frac{2}{D\Delta t}-\frac{2}{\Delta r^2}\right)+M_{i+1,j}^{n}\left(\frac{1}{2r\Delta r}+\frac{1}{\Delta r^2}\right)+M_{i-1,j}^{n}\left(\frac{1}{\Delta r^2}-\frac{1}{2r\Delta r}\right) \tag{7b}$$

$$\lambda=\frac{D\Delta t}{\left(\Delta r^2+\Delta r^2\Delta\theta^2\right)} \tag{7c}$$

Besides, to assure the convergence of the ADI method, similar with the works of Kaya et al. [22,32], the under-relaxation parameter of $\lambda = 0.5$ is adopted in the computations. Since λ is a function of the moisture diffusivity and the time step (Δt) in the drying period (Eq. (7c)), extended run-times in the computations arose due to regulating Δt in accord with the diffusivity level.

3. Results and discussion

The fluid flow and hydrodynamic boundary layer development aspects, surface heat transfer rates and thermal boundary layer structure and mass transfer characteristics, of a circular cylinder with a diameter of $d = 0.04$ m and a temperature of $T_s = 293$ K, are computationally investigated by gathering the necessary data from the latest available research reports [5–8,12,19,20,22,23,27,33–35]. The present analysis is performed for the Reynolds number case of $Re_d = 40$, with the duct inlet (Fig. 1(a)) average air velocity and temperature values of $U_\infty = 1.57 \times 10^{-2}$ m/s and $T_\infty = 333$ K and air and cylinder moisture amounts of $M_a = 0.1$ kg/kg and $M_{cyl} = 3$ kg/kg, being similar to those by [7,12,19,20,22,23,33–35]. Considering the data collection of Panagiotou et al. [27], moisture diffusivity range is decided as $D = 1 \times 10^{-8}$–1×10^{-5} m^2/s; besides blockage is structured in the study with the frequently applied [5–8] values of $\beta = 0.333$–0.800. Fluid flow and momentum transfer mechanisms are demonstrated through streamlines, velocity profiles, separation locations, surface static pressures and wall shear stresses. The heat transfer schemes are discussed in terms of convective heat transfer coefficients and temperature distributions. The effects of blockage ratio and moisture diffusivity on mass transfer characteristics are presented by mass transfer coefficients, drying times, iso-moisture contours and local drying characteristics.

3.1. Computational analysis in the air flow domain

Since comprehensive numerical analyses have been performed throughout the study, the computational output based results presented here aim not only to clarify the current findings of the work but also to validate the sensitivity and accuracy of the calculations. The streamline formation around the cylinder and velocity profiles at the front and back sides of the cylinder for the blockage ratio range of $\beta = 0.333$–0.800 are displayed Fig. 2. Due to the symmetric layout of the streamlines (Fig. 2(a)) around the centerline, upstream, throat and downstream streamlines schemes are plotted for the upper half fluid domain only, where this symmetric evaluation is also a very dependable confirmation of the complete results regarding the momentum transfer analysis. Fig. 2 (a) clearly exhibits for the cases of $\beta = 0.571$–0.800 that, blockage has potency to hydrodynamically force the streamlines to keep their route up to the neighborhood of the cylinder surface and to follow tangent paths to the front face of the cylinder. However, in the low β case of $\beta = 0.333$ the centerline streamlines depart from their lines easily at the upstream section of the flow domain. In higher blockage cases ($\beta = 0.571$–0.800) on the front face of the cylinder the tangent paths, thus the smoothly moving behavior, of the upstream streamlines are strong evidences of higher friction coefficients, static pressures and thermal activity. For the complete blockage cases considered, towards the throat, the flow movement is significantly dominated by the converging style of the physical boundaries resulting in augmented velocity values and fuller velocity profiles. As a consequence, thinner and strictly attaching boundary layers and favorable pressure gradients coincide exactly with the above determinations on streamline formation. Moreover, similar to [5,7,36–39], the separation locations (θ_s) are measured in the counterclockwise direction, with the origin of S_2 (Fig. 1(b)). Computations shown that the separation point shifts downstream with the increase of blockage, where the denoting numbers are $\theta_s = 50.20°$, $41.98°$ and $37.30°$ for $\beta = 0.333$, 0.571 and 0.800 respectively. Flows around circular cylinders without blockage were taken into consideration by many numerical and experimental research studies. The separation location findings of the investigations that considered the unconfined flow for the specific case of $Re = 40$ [5,36–40] were quite similar being in the range of $\theta_s = 53.1°$–$53.8°$. Among the considerably fewer work on flows with blockage, Chakraborty et al. [5] and Sen et al. [7] handled the $Re = 40$ flow around CCs. Either of the research computationally determined the shift of separation towards downstream. As the interpreting outputs are $\theta_s \approx 50°$ ($\beta = 0.333$), $\theta_s \approx 48°$ ($\beta = 0.500$) and $\theta_s \approx 45°$ ($\beta = 0.650$) in [5], those of [7] were reported as $\theta_s \approx 46°$ ($\beta = 0.333$), $\theta_s \approx 37.5°$ ($\beta = 0.500$) and $\theta_s \approx 26.5°$ ($\beta = 0.800$). It can be seen that a scientific agreement is not available between [5] and [7]; the present findings more resemble those of Chakraborty et al. [5]. On the other hand, the rise of maximum

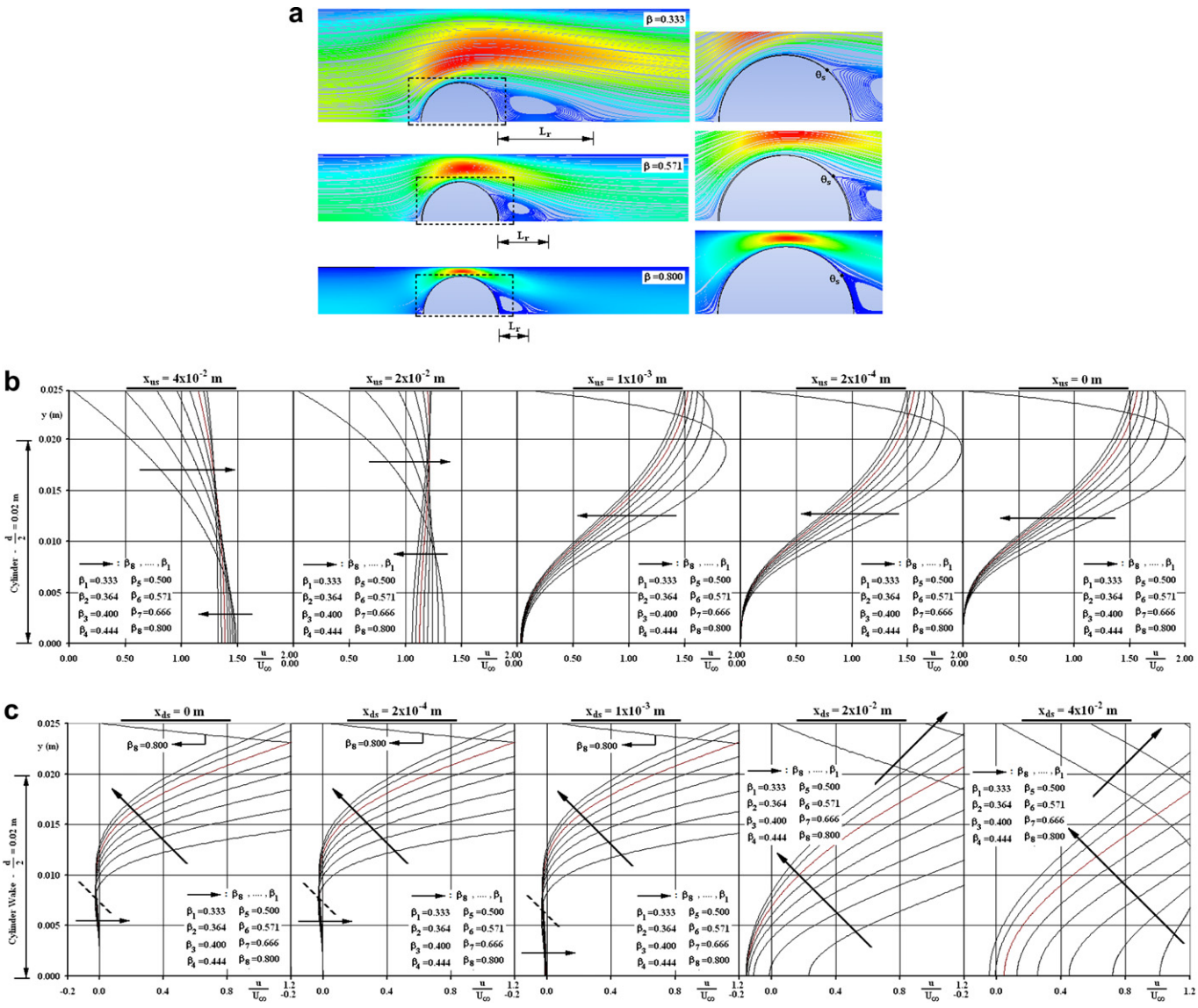

Fig. 2. (a) Streamline formation around the cylinder and (b) upstream and (c) downstream dimensionless velocity profiles for the blockage ratio range of $\beta = 0.333–0.800$.

velocity values at the throat with blockage can be clarified by the computed values of $U_{\text{th-max}} = 3.27 \times 10^{-2}$ m/s $(U/U_\infty = 2.083)$, $U_{\text{th-max}} = 5.05 \times 10^{-2}$ m/s $(U/U_\infty = 3.217)$ and $U_{\text{th-max}} = 1.09 \times 10^{-1}$ m/s $(U/U_\infty = 6.943)$ for $\beta = 0.333$, 0.571 and 0.800 respectively. The zoomed plots of Fig. 2(a) display the vortex layout, downstream of the cylinder. It can not only be inspected from the plots that the onset of these vortices is the separation points but also the vortex influenced domain turns out to be narrower at higher blockage. Particularly defining, the lengths of the recirculation zones are computed as $L_r = \sim 47.3$ mm, ~ 26.9 mm and ~ 16.7 mm for $\beta = 0.333$, 0.571 and 0.800 respectively. These recirculation lengths put forward that the influential domain and strength of the downstream vortex system decreases at high β. Chakraborty et al. [5] for the blockage range of $\beta = 0.050–0.650$, Griffith et al. [6] for the blockage range of $\beta = 0.050–0.900$ and Sen et al. [7] for the blockage range of $\beta = 0–0.800$ reported similar findings on shorter recirculation zones with higher blockage.

Fig. 2(b) presents the dimensionless velocity profiles for the blockage ratio range of $\beta = 0.333–0.800$ and in the upstream domain of $x_{us} = 4 \times 10^{-2}–0$ m, where $x_{us} = 4 \times 10^{-2}$ m is chosen to be equal to the cylinder diameter (d). It can be inspected from the figure that the hydrodynamic response of the flow to the cylinder becomes apparently sensible for $x_{us} \leq 2 \times 10^{-2}$ m ($\sim$d/2), where the dimensionless centerline velocity values drop below the characteristic duct flow value (Fig. 1(a)) of $U/U_\infty = 1.50$ to $U/U_\infty = 1.06$, 1.24 and 1.35 for $\beta = 0.333$, 0.571 and 0.800 respectively. These values and Fig. 2(b) put forward that the presence of the cylinder causes the strongest flow deceleration in the centerline in low β cases. This outcome can be clarified by the dimensionless velocity profiles at $x_{us} = 4 \times 10^{-2}$ m and 2×10^{-2} m. Since $y = \pm 0.025$ m corresponds to the duct walls for $\beta = 0.800$, flow attains relatively low velocities in the neighborhoods and the continuity equation can only be satisfied by the higher velocities away from the duct walls, more specifically in the vicinity of the centerline. Similar impacts, weaker than that of the $\beta = 0.800$ case, are also present in lower blockage applications. As the duct walls are fairly separated in low β cases ($y = \pm 0.035$ m for $\beta = 0.571$ and $y = \pm 0.060$ m for $\beta = 0.333$) their impact to the centerline momentum rates are milder. In the last 2.5% d upstream section of the flow domain ($x_{us} \leq 1 \times 10^{-3}$ m), the role of the cylinder on the hydrodynamic behavior of the flowing air becomes noticeable. Such that for $\beta = 0.333$, 0.571 and 0.800 the dimensionless centerline velocity

values are computed as $U/U_\infty = 0.027$, 0.036 and 0.045 at $x_{us} = 1 \times 10^{-3}$ m and $U/U_\infty = 0.002$ ($\beta = 0.333$–0.800) at $x_{us} = 2 \times 10^{-4}$ m. These values detail the late hydrodynamic response of the flow at high β cases, which results in the rapid deceleration of the flowing air to zero towards the stagnation point ($x_{us} = 1 \times 10^{-3}$ m $\rightarrow x_{us} = 0$ m). Fig. 2(b) additionally shows that the throat ($y \geq 0.02$ m) velocity profiles of $x_{us} \leq 1 \times 10^{-3}$ m for $\beta = 0.333$–0.800 resemble fuller forms with the increase of β. Such that, on the cylinder projection lines ($y = \pm 0.02$ m) computations resulted in the U/U_∞ ranges of $1.31 \rightarrow 1.33$, $1.60 \rightarrow 1.66$ and $1.84 \rightarrow 2.00$ ($x_{us} = 1 \times 10^{-3}$ m $\rightarrow x_{us} = 0$ m) for $\beta = 0.333$, 0.571 and 0.800, clarifying the rise of velocity values at higher β cases upstream of the throat. The wider U/U_∞ ranges at high β, together with the presented streamlines of Fig. 2(a), point out the onset of flow acceleration at the throat upstream, which will cause the static pressure values to decrease in the flow direction, downstream shift of the separation point, thinner boundary layer formation and higher frictional activity and heat transfer rates on the cylinder surface.

The downstream ($x_{ds} = 0$–4×10^{-2} m) dimensionless velocity profiles for the blockage ratio range of $\beta = 0.333$–0.800 are shown in Fig. 2(c). The computed velocity profiles display that backflow ($U/U_\infty < 0$) exists in the downstream section of the cylinder in spite of the level of applied blockage. Thus, to clarify the impact of blockage on the downstream momentum transfer, vortex strength and the downstream velocities profiles, discussions through Fig. 2(c) are structured in conjunction with the vortex structures of Fig. 2(a). In the vicinity of the cylinder back-face ($x_{ds} \leq 1 \times 10^{-3}$ m) the peak values of the dimensionless velocities are located at $y = \pm \sim 8.37 \times 10^{-3}$, $\pm \sim 8.16 \times 10^{-3}$ and $\pm \sim 7.18 \times 10^{-3}$ m for $x_{ds} = 0$, 2×10^{-4} and 1×10^{-3} m respectively. As the U/U_∞ values of the $\beta = 0.333$ case at these downstream locations are -0.0216, -0.0223 and -0.0239, they drop down to -0.0192, -0.0201 and -0.0225 at $\beta = 0.800$. The almost unvarying nature of the dimensionless velocity data express deviations in the centerline neighborhood towards the downstream location of $x_{ds} = 1 \times 10^{-3}$ m with the U/U_∞ values of $0 \rightarrow -0.0039$ ($x_{ds} = 0 \rightarrow 1 \times 10^{-3}$ m) for $\beta = 0.333$ and $0 \rightarrow \times 0.0128$ for $\beta = 0.800$. The complete set of values for $0 \leq x_{ds} \leq 1 \times 10^{-3}$ m indicate that at the backside vicinity of the cylinder the role of the blockage is dominant to the impact of solid-fluid interaction on the flow domain such that the influence of the downstream vortex system can be considered secondary. The suppressed adverse pressure gradients, downstream shifted separation points and Fig. 2(a) and (c) simultaneously put forward and verify that the role of blockage on the vortex strength and structure is extremely determinative. The present computational evaluations are in agreement with the circular cylinder findings of Sen et al. [7] ($\beta = 0$–0.800) and Buyruk et al. [15] ($\beta = 0.180$–0.470) from the point of the role of blockage on the downstream flow domain and wake velocity profiles. Computations further identified the vortex width values as $y = \pm 0.0160$ m, $y = \pm 0.0124$ m and $y = \pm 0.0110$ m ($x_{ds} = 0$ m) for $\beta = 0.333$, $\beta = 0.571$ and $\beta = 0.800$ respectively. Moreover, at certain locations in the flow domain the order of the velocity profiles (for different β cases) is inverted. These locations are indicated by dashed lines in Fig. 2(c) and are determined as ± 0.0079, ± 0.0076 and ± 0.0064 m at $x_{ds} = 0$, 2×10^{-4} and 1×10^{-3} m. Both the above vortex width values and the invert points of the velocity profiles clarify not only the narrower vortex formation at high blockage cases but also the narrowing manner of the vortices in the downstream direction.

Fig. 3(a) displays the throat and downstream temperature contours for the blockage ratio cases of $\beta = 0.333$, 0.571 and 0.800. The present analysis put forward that in the high blockage cases, hot fluid domains, in the cylinder vicinity, become thinner and get closer to the cylinder surface, which can be attributed to the presented (Fig. 2) forced hot fluid-cylinder contact at higher β, where the growth of this interaction is likely to produce higher surface heat transfer rates. The zoomed plots of Fig. 3(a) clearly identify that with the increase of blockage the thermal boundary layer gets thinner up to the separation point (θ_s). It can be inspected from Fig. 3(a) that thermal boundary layer thickens beyond the separation point in the complete blockage cases. However, the zoomed plots further shows that towards $\theta = 180^\circ$, the isotherm contours of the cases with $\beta = 0.333$ and $\beta = 0.571$ display comparable layouts, which may be accounted for similar thermal activity in the corresponding cylinder surface sections. On the other hand, when compared to those of milder blockage cases, the thermal boundary layer resembles a thicker formation for $\theta > \theta_s$ at $\beta = 0.800$. The fundamentals of this outcome can be interrelated with two issues: (i) the narrowing nature of the downstream vortex system disturbs the boundary layer and weakens the fluid-solid contact and (ii) the existence of the highest backward velocity values at $\beta = 0.800$ (Fig. 2(c)). These determinations clarify the interrelation of hydrodynamic and thermal activities around the circular cylinder. Similar with the present findings on the deviation of the isotherm structure with blockage, Buyruk et al. [15] also depicted analogous information for the wake of a cylinder.

Upstream dimensionless temperature values (ζ – Eq. (6h)), for the blockage ratio range of $\beta = 0.333$–0.800 are demonstrated in Fig. 3(b). Computations show that, in the complete blockage range, thermal characteristics and the flow temperature values almost unchanged ($\zeta = \sim 1.00$) up to the section of $x_{us} = 1 \times 10^{-2}$ m in spite of the presence of the cylinder. As the flow gets closer to the cylinder ($x_{us} = 1 \times 10^{-2} \rightarrow 0$ m) promoted thermal activity and sensible drops in the temperature values are evaluated. From the point of flow temperature-blockage interaction, the numerical analysis pointed out the rise of temperature values with higher blockage, indicating thinner thermal boundary layer development with higher blockage. It can also be inspected from the figure that temperature values considerably decrease as the flow approaches the stagnation point ($x_{us} = 0$ m and $\theta = 0^\circ$); such that as the centerline dimensionless temperature range at $x_{us} = 1 \times 10^{-3}$ m is computed as $\zeta = 0.220 \rightarrow 0.187$ for $\beta = 0.800 \rightarrow 0.333$, the corresponding values are $\zeta = 0.006 \rightarrow 0.005$ at the stagnation point. Indeed these evaluations expose the reaction parallelism of the thermal and hydrodynamic boundary layers when interacting with blockage effects and as well reveal the foresights on the augmentation of heat transfer rates at higher blockage.

Fig. 3(c) shows the dimensionless temperature profiles for the downstream domain of $x_{ds} = 0$–4×10^{-2} m. The present computational outputs of Fig. 3(c) are essential in characterizing the downstream heat transfer fundamentals and the roles of blockage and vortex formation (Fig. 2) on the downstream temperature distribution. For the complete β range considered, the superiority of the stagnation point ($\theta = 0^\circ$ and $x_{us} = 0$ m) dimensionless temperature values ($\zeta \approx 0.0055$) (Fig. 3(b)) to those of the $\theta = 180^\circ$ and $x_{ds} = 0$ m ($\zeta \approx 0.0012$) (Fig. 3(c)), puts forward that in spite of the heat transfer enhancing capability of the downstream vortex system (Fig. 2(a)–(c)), the momentum, in the vicinity of the stagnation point, has major potential to bring about significantly augmented heat transfer rates. On the other hand, as the isotherms of Fig. 3(a) point out, the high blockage of $\beta = 0.800$ results in a unique temperature distribution when compared to those of the lower blockage cases. The zoomed plots clarify that in the neighborhood of $\theta = 180^\circ$ and $x_{ds} = 0$ m the dimensionless temperature values of the confined flow cases of $\beta = 0.333$–0.666 are resembling especially within the separated vortex domain of $x_{ds} = 0$–1×10^{-3} m (Fig. 2(a)). The similar structure of the thermal layouts of $\beta = 0.333$–0.666 cases is a trustable foresight for comparable heat transfer in the corresponding region. However the

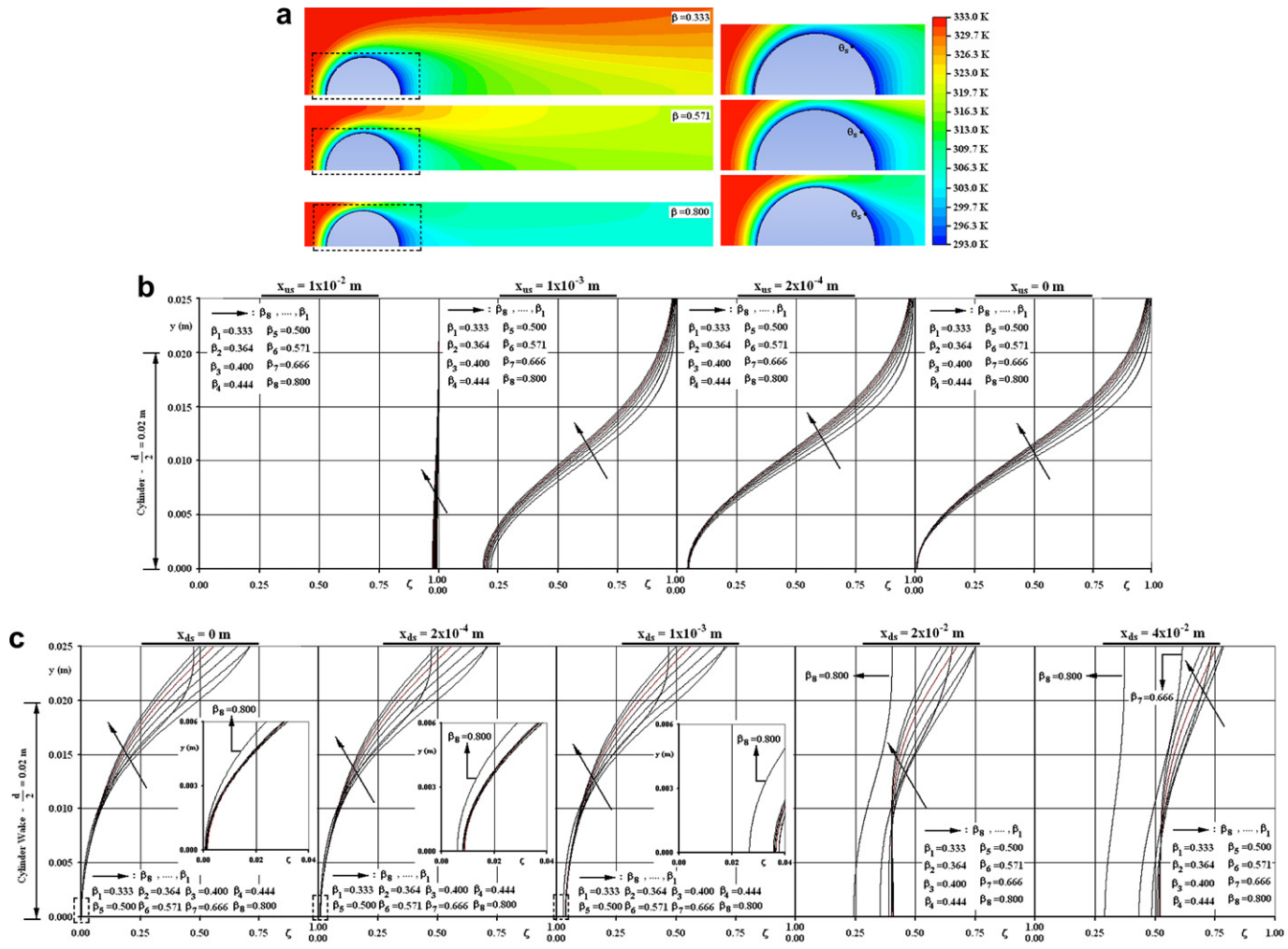

Fig. 3. (a) Temperature contours around the cylinder and (b) upstream and (c) downstream dimensionless temperature profiles for the blockage ratio range of $\beta = 0.333–0.800$.

ζ of $\beta = 0.800$ come out to be lowest for the complete blockage range, where the narrower temperature gap among the flow and cylinder results in a mild temperature gradient thus lower heat transfer rates in that section of the cylinder surface. In the further downstream regions ($x_{ds} \geq 2 \times 10^{-2}$ m) the individual behavior of the thermal distribution of the $\beta = 0.800$ case becomes more apparent. Moreover, at the one cylinder diameter distance of $x_{ds} = 4 \times 10^{-2}$ m, the dimensionless temperature profile of $\beta = 0.666$ as well deviates from those of $\beta = 0.333–0.571$, which indicates that the exceptional thermal character of each confined flow case becomes more noticeable in the downstream direction. This outcome can scientifically be detailed by rationalizing the issue of downstream distance in conjunction with the recirculation length (L_r). As L_r is shown to become shorter with high β, the impact of blockage on thermal activity of the separated domain comes into sight even in the neighborhood of the contact plane of the cylinder and downstream vortex system. On the other hand, the contrary evaluation can be set for low blockage scenarios with wider recirculation zones. These findings imply that besides demonstrating the impact of β on ζ, Fig. 3(c) as well presents the influence of downstream vortex formation on the flow temperature distribution.

The angular variations of surface static pressures (P_s), wall shear stresses (τ_w) and convective heat transfer coefficients (h_θ) for the blockage ratio range of $\beta = 0.333–0.800$ are displayed in Fig. 4. Static pressure values are evaluated to significantly grow with blockage on the cylinder front-face; such that as the lowest blockage of $\beta = 0.333$ results in the static pressure value of $P_s = 8.57 \times 10^{-4}$ Pa ($C_p = 5.91$), the corresponding outputs for the $\beta = 0.666 \rightarrow 0.800$ range become $P_s = 4.05 \times 10^{-3}$ Pa $\rightarrow 1.33 \times 10^{-2}$ Pa ($C_p = 27.93 \rightarrow 91.81$). Similar with the present determinations, the circular cylinder research of Chakraborty et al. [5] for $Re < 200$ with $\beta = 0.05–0.65$, Buyruk et al. [15] for $120 < Re < 390$ with $\beta = 0.18–0.47$, Sharma and Eswaran [18] for $50 < Re < 150$ with $\beta = 0.10–0.50$ and Khan et al. [16] with $\beta = 0.10–0.90$ and the square cylinder investigation of Dhiman et al. [17] for $Re < 45$ with $\beta = 0.125–0.25$ also pointed elevated P_s and C_p with β. Numerical outputs further show that static pressure values drop as the flow approaches the throat ($\theta = 90°$), which can be explained by the rise of dynamic pressures due to the acceleration of flow in that comparably narrow fluid domain, resulting in the opposite impacts on the static pressures. Downstream of throat, P_s values attain the minimum values at $\theta_{P_s-min} = 93.5° \rightarrow 109.9°$ ($\beta = 0.333 \rightarrow 0.800$). The present computations additionally designate not only that the minimum static pressure values are located upstream of the separation points (θ_s) but also that the minimum P_s locations appear at further angular positions in high β cases, which can be enlightened through the above discussion on the determinedly attaching boundary layer and delayed separation in these scenarios (Fig. 2(a) and (b)).

Fig. 4(b) presents the wall shear stress values on the cylinder surface. Numerical outputs signify for the overall cylinder surface

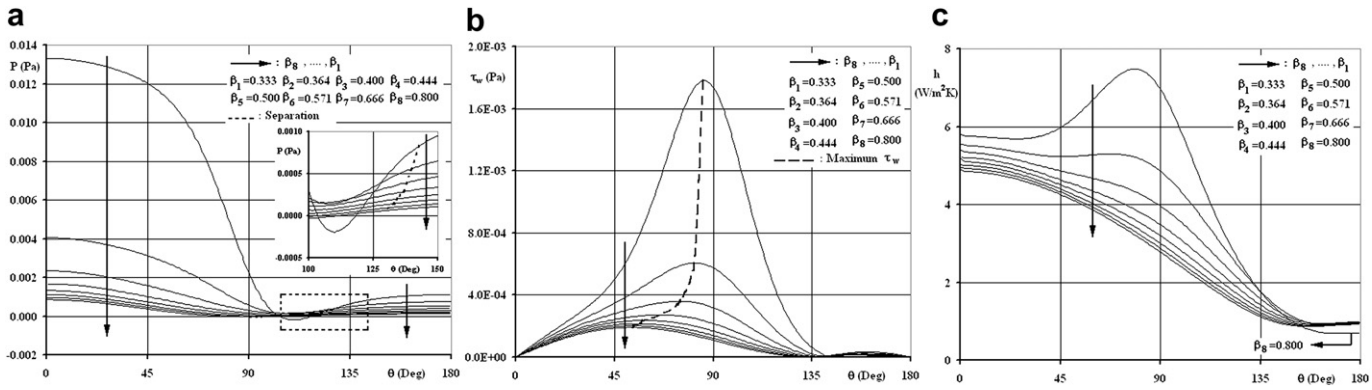

Fig. 4. Variation of (a) static pressures, (b) wall shear stresses and (c) convective heat transfer coefficients on the cylinder surface for the blockage ratio range of $\beta = 0.333–0.800$.

that higher blockage excites wall shear stress values, where this increase can be associated with the fuller velocity profiles, strongly adjacent streamlines to the cylinder and the forced fluid-wall contact (Fig. 2) at high blockage flows. The growing nature of frictional activity at high β was also reported by Chakraborty et al. [5], Khan et al. [16] and Dhiman et al. [17]. Besides, simultaneous consideration of the angular variations of P_s and τ_w enlightens that at the angular positions, where the style of the P_s curves adjusts to converge to the minimum P_s values (Fig. 4(a)), maximum τ_w are located (Fig. 4(b)). On the other hand, computations identified the maximum shear stress locations as $\theta_{\tau_w-max} = 53.4°$ and 85.4° for $\beta = 0.333$ and 0.800, pointing out that higher β shifted the θ_{τ_w-max} downstream. The present evaluations on the locations of maximum frictional activity do not show parallelism with the works of Khan et al. [14] ($\theta_{C_f-max} = \sim 58°$) for $\beta = 0$ and Schonauer [41] ($\theta_{C_f-max} = \sim 57°$) for $\beta = 0$, but they are in harmony with the findings of Khan et al. [16] ($\theta_{C_f-max} = \sim 60°$) for $\beta = 0.4$ and Zukauskas and Ziugzda [42] ($\theta_{C_f-max} = \sim 50°$) for $\beta = 0$. The delay of separation with blockage and the no shear (frictionless) behavior in the separated flow domain can also be recognized in Fig. 4(b).

Fig. 4(c) displays the variation of convective heat transfer on the cylinder surface. The augmenting impact of blockage on surface heat transfer rates can be seen from the plot. The average convective heat transfer coefficients (h_θ) are computed as $h_{ave} = 2.76$, 3.38 and 4.43 W/m^{2}K for the blockage ratio cases of $\beta = 0.333$, 0.571 and 0.800, where the corresponding average Nusselt numbers are $Nu_{ave} = 4.05$, 4.97 and 6.51. Biswas and Sarkar [37], Dennis et al. [43], Jafroudi and Yang [44] and Apelt and Ledwich [45] considered flows around circular cylinders without blockage for the specific case of $Re = 40$ and evaluated average Nusselt numbers in the narrow band of $Nu_{ave} = 3.20–3.48$. On the other hand, Bharti et al. [12], Buyruk et al. [15], Khan et al. [16] and Dhiman et al. [17] also reported raised heat transfer values with blockage. Fig. 4(c) additionally points out that heat transfer rates at different angular positions on the cylinder are influenced by blockage at different intensities; such that as the $h_{\beta=0.800}/h_{\beta=0.333}$ and $h_{\beta=0.571}/h_{\beta=0.333}$ ratios attain the values of 1.19 and 1.11 at the stagnation point ($\theta = 0°$), they become 1.40 and 1.12 at $\theta = 45°$ and 2.51 and 1.42 at the throat ($\theta = 90°$). The growing impact of blockage on the heat transfer characteristics, towards the throat, can evidently be identified from these comparisons. The thinner front-face boundary layer development due to higher blockage (Fig. 2(a) and (b)) causes the forced interaction of the flow with the cylinder surface, which in return, similar to the frictional activity (Fig. 4(b)), also enhances the thermal actions. Ozalp's [46] computational investigations on internal micro-duct flows and Umur and Ozalp's [47] experimental external flat and curved flow measurements pointed the augmenting impact of thinner boundary layers on the heat transfer rates. Many other external and internal flow researches [48,49] as well concluded with matching determinations. It can further be seen from Fig. 4(c) that, minimum heat transfer rates are evaluated downstream of the separation points. The almost constant heat transfer values in the angular domain of $\sim 162° < \theta < 180°$, are generated by the nearly constant temperature field in the downstream vortex domain (Fig. 3(c)). On the other hand, Fig. 4(c) further indicates for the cylinder surface section of $\sim 162° < \theta < 180°$ that the surface heat transfer rates of the blockage range $\beta = 0.333–0.666$ are quite similar. This outcome can be attributed to the comparable combined impact of blockage and downstream vortex system on the heat transfer mechanism. However at the highest blockage of $\beta = 0.800$, as enlightened through Fig. 2(a), the strength of the downstream vortex reduces, which as a consequence negatively affects the heat transfer rates. Besides being lower in magnitude, the influential region of the constant heat transfer values becomes narrower ($\sim 166° < \theta < 180°$), which can scientifically be linked to the thinner vortex formation at $\beta = 0.800$ (Fig. 2(a)). Further detailing the back-face of the cylinder points out that, as the $h_{\beta=0.800}/h_{\beta=0.333}$ and $h_{\beta=0.571}/h_{\beta=0.333}$ ratios get the values of 1.58 and 1.40 at $\theta = 135°$, they become 0.76 and 1.07 at $\theta = 180°$. Since the throat ($\theta = 90°$) ratios come out to be superior on the complete cylinder surface, it can be concluded that the impact of boundary layer thinning is dominant to the role of the vortex structure on the heat transfer mechanism. Discussing the overall heat transfer rates of the cylinder indicates that h_{ave} rises by 22.5% and 60.5% among the $\beta = 0.333 \rightarrow 0.571$ and $\beta = 0.333 \rightarrow 0.800$ scenarios respectively.

3.2. Computational analysis in the moist cylinder domain

The variation of surface mass transfer coefficients (h_m) of the circular cylinder, subjected to confined flow, is essential in determining the mass transfer behavior. In accordance with the Lewis analogy [30], the scientific link between h_θ and h_m is assembled into the analysis through Eq. (6i), which was as well employed by Kaya et al. [22]. The evaluated h_m variations on the cylinder surface are plotted in Fig. 5 for the blockage ratio and diffusivity ranges of $\beta = 0.333–0.800$ and $D = 1 \times 10^{-5}–1 \times 10^{-8}$ m^2/s. From the figure it can not only be inspected that lower moisture diffusivity values distinctly reduce h_m on the complete cylinder surface, but can also be identified that mass transfer coefficients increase with blockage, except in the narrow region of $\sim 162° < \theta < 180°$ for the particular case $\beta = 0.800$. Moreover, to clarify the individual and combined roles of β and D on h_m, overall mean ($\overline{h}_m$), front face mean ($\overline{h}_{m\text{-}ff}$) and back face mean ($\overline{h}_{m\text{-}bf}$) mass transfer coefficients are given in Table 2. From the tabulated data it can be resolved that, being independent of moisture diffusivity, as the $\overline{h}_{m\text{-}ff}/\overline{h}_m$ and $\overline{h}_{m\text{-}bf}/\overline{h}_m$

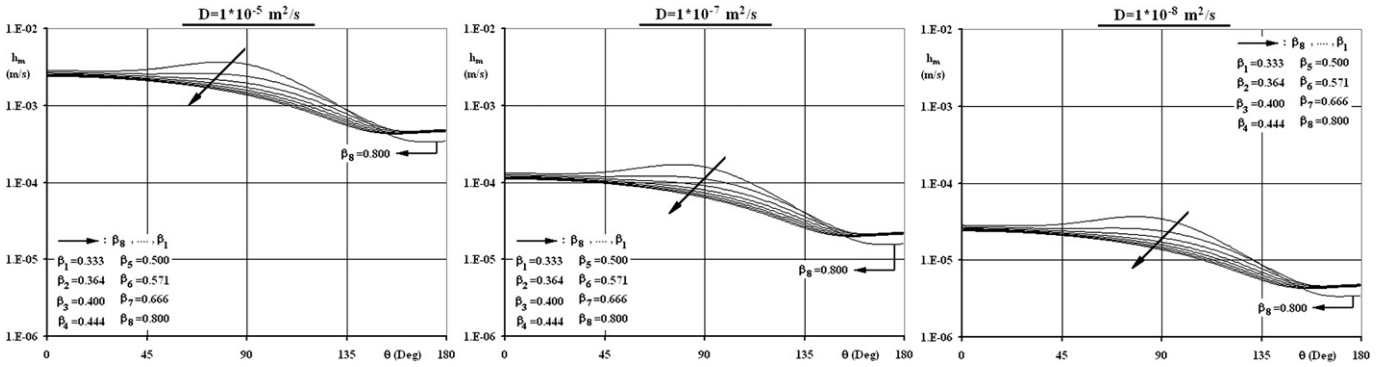

Fig 5. Variation of mass transfer coefficients for the moisture diffusivity and blockage ratio ranges of $D = 1 \times 10^{-5}$–1×10^{-8} m^2/s and $\beta = 0.333$–0.800.

ratios attain the values of ~1.43 and ~0.57 for $\beta = 0.800$, they turn into ~1.49 and ~0.51 for $\beta = 0.333$. These ratios clarify that the rise of $\overline{h}_{\text{m-bf}}$ is dominant to that of $\overline{h}_{\text{m-ff}}$ resulting in the grow of $\overline{h}_{\text{m-bf}}/\overline{h}_{\text{m}}$ and fall of $\overline{h}_{\text{m-ff}}/\overline{h}_{\text{m}}$ with higher β. Being complementary to those plotted in Fig. 5, the present discussions and the tabulated values point out the following issues: (i) Both the back ($\overline{h}_{\text{m-bf}}$) and front ($\overline{h}_{\text{m-ff}}$) face mass transfer coefficients are elevated by higher blockage, (ii) Mass transfer coefficients are reduced by lower moisture diffusivity values in the complete blockage ratio range, (iii) The superior rank of $\overline{h}_{\text{m-ff}}$ above $\overline{h}_{\text{m}}$ and $\overline{h}_{\text{m-bf}}$ can be considered as a trustable foresight for the enhanced moisture transfer characteristics on the front-face of the cylinder.

Overall drying times (Δt_{od}) for the moisture diffusivity and blockage ratio ranges of $D = 1 \times 10^{-5}$–1×10^{-8} m^2/s and $\beta = 0.333$–0.800 are shown in Fig. 6. The augmentation of heat transfer rates at higher blockage cases (Fig. 4(c)) in return caused the rise of mass transfer coefficients (Fig. 5), which as well resulted in the lower Δt_{od}. Besides, as moisture diffusivity stands for the moisture transfer capability of the material, higher D also enumerated lower overall drying times. The visual inspections through Fig. 6 can be numerically assured by the following figures: The Δt_{od} for the weakest blockage of $\beta_1 = 0.333$ are computed as 59250, 6755.2, 858.86 and 124.15 seconds for $D_1 = 1 \times 10^{-8}$ m^2/s, $D_2 = 1 \times 10^{-7}$ m^2/s, $D_3 = 1 \times 10^{-6}$ m^2/s and $D_4 = 1 \times 10^{-5}$ m^2/s respectively. For the strongest blockage ($\beta_2 = 0.800$) these numbers decrease to 57402, 6329.6, 766.12 and 103.55 seconds for the identical moisture diffusivities. Fig. 6 and the presented Δt_{od} values simultaneously put forward that especially for $D < 1 \times 10^{-7}$ m^2/s the overall drying times significantly expand. This evaluation is supported by the ratio of the overall drying times, among different diffusivity levels, as $\Delta t_{od-D_3}/\Delta t_{od-D_4} = 6.92 \rightarrow 7.40$, $\Delta t_{od-D_2}/\Delta t_{od-D_3} = 7.87 \rightarrow 8.26$ and $\Delta t_{od-D_1}/\Delta t_{od-D_2} = 8.77 \rightarrow 9.07$ ($\beta = 0.333 \rightarrow 0.800$). Since moisture diffusivity property can be as low as $D = 1 \times 10^{-15}$ m^2/s [27], the present determination is considerably significant for drying applications from the point that the drying of a product, with a low moisture diffusivity, can take extremely a long time. Additionally, the rise of the ratios with higher blockage points out that the influence of moisture diffusivity on overall drying times advances with stronger blockage. From the above Δt_{od} values, the impact of blockage can additionally be defined by the ratio of $\Delta t_{od-\beta_1}/\Delta t_{od-\beta_2}$, where the outcomes for the diffusivity cases of D_1, D_2, D_3 and D_4 are quantified as 1.032, 1.067, 1.121 and 1.199 respectively. The grow of these figures with higher moisture diffusivity establishes the scientific fact that, at high D cases, β motivates the mass transfer activity more potentially.

Fig. 7 demonstrates the variation of dimensionless moisture contents on cylinder-average (ϕ_{a}) and cylinder-center (ϕ_{c}) basis for the blockage ratio and moisture diffusivity ranges of $\beta = 0.333$–0.800 and $D = 1 \times 10^{-5}$–1×10^{-8} m^2/s, with the notation that as $\phi = 1.00$ indicates the initial ($t = 0$ s) moisture content, $\phi = 0.00$ designates the dry product ($t = \Delta t_{\text{od}}$). It can be inspected from the figure that, center moisture levels (Fig. 7(b)) are higher than those of the average values (Fig. 7(a)), where the gap becomes more considerable in low diffusivity cases. The noticeable influence of moisture diffusivity on the local moisture levels identifies the necessity of considering both the center and average moisture levels, while deciding the drying period. Besides, setting the period of drying is also essential from the point of operation cost in industrial applications. The present computations as well bring forth that the first half of the overall drying time ($\Delta t_{\text{od}}/2$) is more important than the later period due to the fact that only 1.5–2.25% of the excess moisture content (M_{cyl}-M_{a}) remains in the cylinder for $t > \Delta t_{\text{od}}/2$. In order to fulfill and support Fig. 7, Table 3 is given to display the $\phi_{\text{c}}/\phi_{\text{a}}$ ratios at 5 instants of the overall drying times and for 2 blockage ratio and 3 diffusivity scenarios. From the tabulated data the following items can be drawn: (i) There exists almost uniform moisture distribution inside the product in the final 5% of the drying period, such that average and center moisture levels have a gap of less than 1.6%, (ii) Due to elevated mass transfer coefficients in higher blockage cases, the gap among the center and average moisture levels are superior to those of the lower blockage cases, (iii) The gap is more remarkable in lower diffusivity products to those of the materials with higher diffusivity, (iv) Being independent of moisture diffusivity and blockage ratio levels, the gap among the center and average moisture content values is maximum in the early stages of the drying process.

Table 2
Variation of overall, front-face and back-face mean mass transfer coefficients for the moisture diffusivity and blockage ratio ranges of $D = 1 \times 10^{-5}$–1×10^{-8} m^2/s and $\beta = 0.333$–0.800.

	$D = 1 \times 10^{-5}$ m^2/s			$D = 1 \times 10^{-7}$ m^2/s			$D = 1 \times 10^{-8}$ m^2/s		
	$\overline{h}_{\text{m}}$(m/s)	$\overline{h}_{\text{m-ff}}$(m/s)	$\overline{h}_{\text{m-bf}}$(m/s)	$\overline{h}_{\text{m}}$(m/s)	$\overline{h}_{\text{m-ff}}$(m/s)	$\overline{h}_{\text{m-bf}}$(m/s)	$\overline{h}_{\text{m}}$(m/s)	$\overline{h}_{\text{m-ff}}$(m/s)	$\overline{h}_{\text{m-bf}}$(m/s)
$\beta = 0.333$	1.36E−03	2.02E−03	6.92E−04	6.30E−05	9.39E−05	3.21E−05	1.36E−05	2.02E−05	6.92E−06
$\beta = 0.444$	1.48E−03	2.17E−03	7.94E−04	6.87E−05	1.01E−04	3.68E−05	1.48E−05	2.17E−05	7.94E−06
$\beta = 0.666$	1.85E−03	2.61E−03	1.09E−03	8.60E−05	1.21E−04	5.07E−05	1.85E−05	2.61E−05	1.09E−05
$\beta = 0.800$	2.18E−03	3.12E−03	1.25E−03	1.01E−04	1.45E−04	5.80E−05	2.18E−05	3.12E−05	1.25E−05

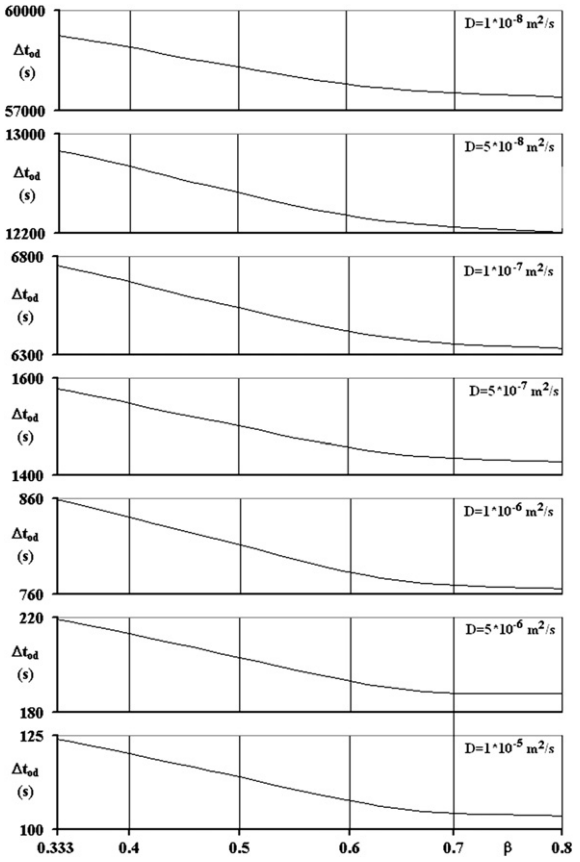

Fig. 6. Variation of overall drying times for the moisture diffusivity and blockage ratio ranges of $D = 1 \times 10^{-5}$–1×10^{-8} m^2/s and $\beta = 0.333$–0.800.

Fig. 8 displays the iso-moisture contours for the blockage ratio cases of $\beta = 0.800$ (Fig. 8(a)), $\beta = 0.666$ (Fig. 8(b)), $\beta = 0.444$ (Fig. 8(c)) and $\beta = 0.333$ (Fig. 8(d)) at the 5% drying times for the moisture diffusivity levels of $D = 1 \times 10^{-5}$ m^2/s, $D = 5 \times 10^{-7}$ m^2/s and $D = 1 \times 10^{-8}$ m^2/s. It can be extracted from the figure that the $\phi_{max\ (\beta=0.333)}$ and $\phi_{max\ (\beta=0.800)}$ values diverge at high D cases; such that as the $\phi_{max\ (\beta=0.333)} - \phi_{max\ (\beta=0.800)}$ difference for $D = 1 \times 10^{-8}$ m^2/s is ~0.001 it grows to 0.011 and 0.026 at $D = 5 \times 10^{-7}$ m^2/s and $D = 1 \times 10^{-5}$ m^2/s respectively. These evaluations put forward the fact that the role of β, and the so occurring h_m distribution, on ϕ_{max} and ϕ_{max} location becomes ineffective at low moisture diffusivities. Computational outputs also clarified the gap of the ϕ_{max} and the moisture levels at surface points of S_1 ($\theta = 0^\circ$) and S_2 ($\theta = 180^\circ$) (Fig. 1(b)): As ϕ_{max} exceeds ϕ_{S_1} and ϕ_{S_2} by $0.915 \rightarrow 0.920$ and $0.772 \rightarrow 0.725$ ($\beta = 0.333 \rightarrow 0.800$) at $D = 1 \times 10^{-8}$ m^2/s, these differences drop down to $0.662 \rightarrow 0.702$ and $0.237 \rightarrow 0.202$ at $D = 1 \times 10^{-5}$ m^2/s. Being consistent with the ϕ_c/ϕ_a ratios of Table 3, these figures not only identify that the gap among the maximum and surface moisture values raises in lower moisture diffusivities cases, but also notify that as the $\phi_{max} - \phi_{S_2}$ difference decreases with higher blockage ratios, the contrary is valid for $\phi_{max} - \phi_{S_1}$. Fig. 8 additionally indicates that as the ϕ_{max} locations are separated from cylinder center in the moisture diffusivity scenario of $D = 1 \times 10^{-5}$ m^2/s, those of $D = 1 \times 10^{-8}$ m^2/s are located at the cylinder center in the complete blockage range considered ($\beta = 0.333$–0.800). This evaluation puts forward that in drying applications with high moisture diffusivities ($D = 1 \times 10^{-5}$ m^2/s) surface mass transfer coefficients (h_m) are quite determinative on the front and back face moisture levels. However in cases with lower diffusivity ($D = 1 \times 10^{-8}$ m^2/s) moisture levels on the front and back faces become similar resulting in the almost symmetric moisture distribution within the cylinder and the shift of ϕ_{max} location to the cylinder center. The mechanism of this evaluation can further be identified through the converging nature of above $\phi_{max} - \phi_{S_1}$ and $\phi_{max} - \phi_{S_2}$ differences in lower moisture diffusivities.

The effects of blockage ratio ($\beta = 0.333$, $\beta = 0.800$) and moisture diffusivity ($D = 1 \times 10^{-5}$ m^2/s, $D = 5 \times 10^{-7}$ m^2/s and $D = 1 \times 10^{-8}$ m^2/s) on the in-time variation of the dimensionless moisture levels at the surface points of S_1 ($\theta = 0^\circ$), S_2 ($\theta = 180^\circ$) and S_3 ($\theta = 90^\circ$) are deduced in Fig. 9. It can be inspected from the figure that, for the complete moisture diffusivity range investigated, as

Table 3
Variation of center to average dimensionless moisture content ratios at 5 instants of the overall drying times for the moisture diffusivity and blockage ratio ranges of $D = 1 \times 10^{-5}$–1×10^{-8} m^2/s and $\beta = 0.333$–0.800.

		ϕ_c/ϕ_a				
		5% Δt_{od}	25% Δt_{od}	50% Δt_{od}	75% Δt_{od}	95% Δt_{od}
$D = 1 \times 10^{-5}$ m^2/s	$\beta = 0.333$	1.358	1.306	1.131	1.026	1.006
	$\beta = 0.800$	1.442	1.380	1.160	1.032	1.007
$D = 1 \times 10^{-7}$ m^2/s	$\beta = 0.333$	1.630	1.547	1.284	1.057	1.013
	$\beta = 0.800$	1.674	1.589	1.301	1.060	1.014
$D = 1 \times 10^{-8}$ m^2/s	$\beta = 0.333$	1.729	1.635	1.339	1.068	1.015
	$\beta = 0.800$	1.759	1.664	1.350	1.070	1.016

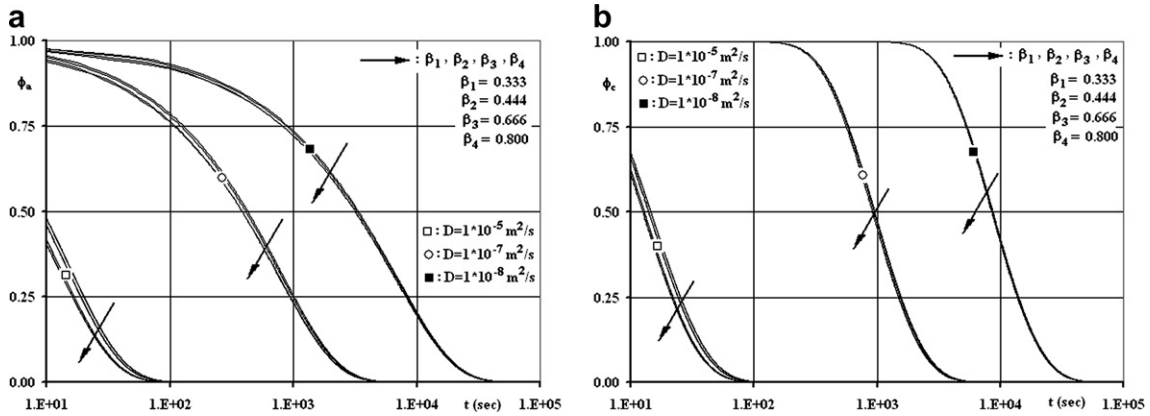

Fig. 7. In time variation of (a) cylinder average and (b) cylinder center dimensionless moisture contents for the moisture diffusivity and blockage ratio ranges of $D = 1 \times 10^{-5}$–1×10^{-8} m^2/s and $\beta = 0.333$–0.800.

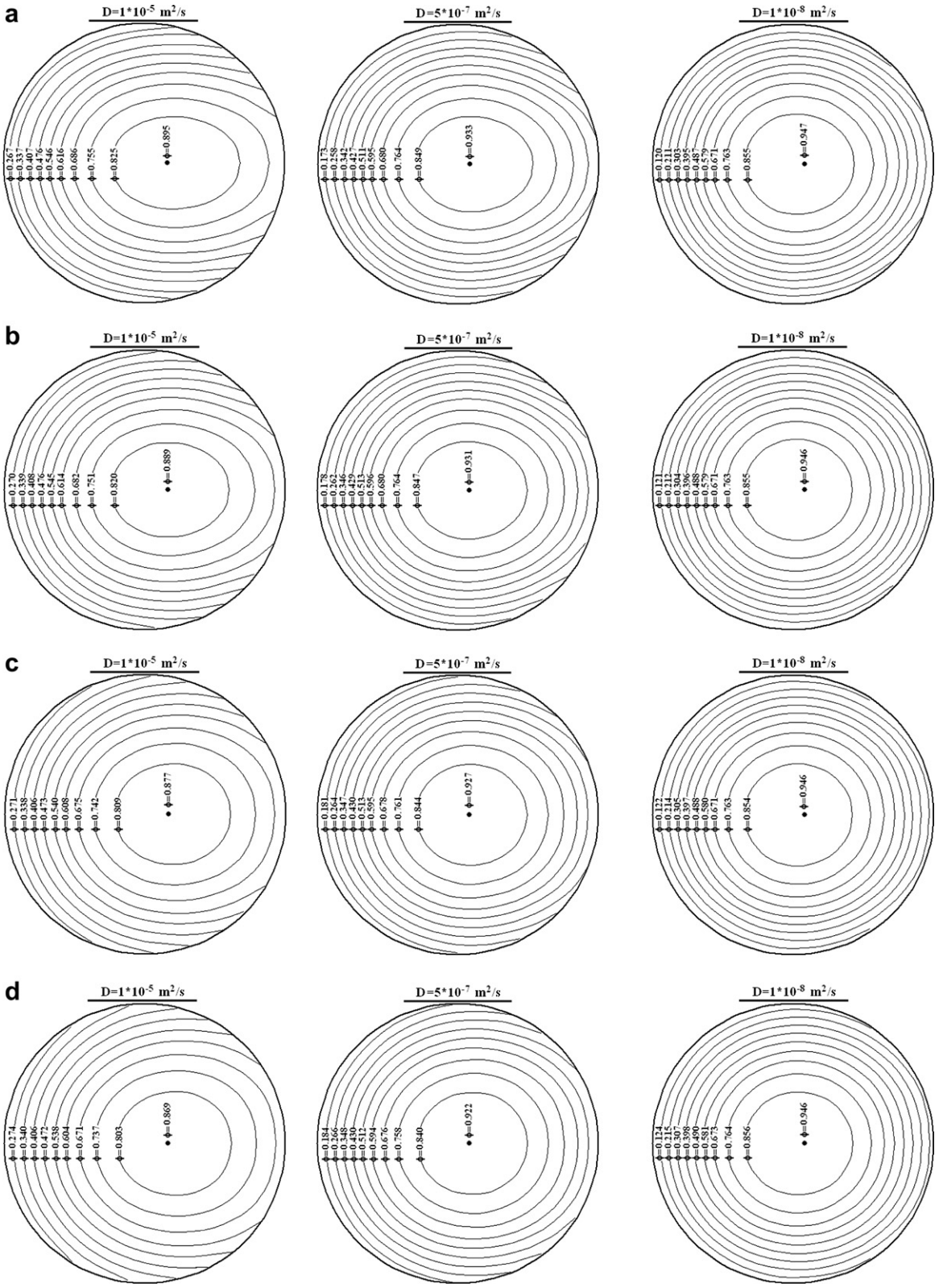

Fig. 8. Iso-moisture contours at the 5% drying times of the cases with $D = 1 \times 10^{-5}$, 5×10^{-7} and 1×10^{-8} m^2/s for the blockage ratios of (a) $\beta = 0.800$, (b) $\beta = 0.666$, (c) $\beta = 0.444$ and (d) $\beta = 0.333$.

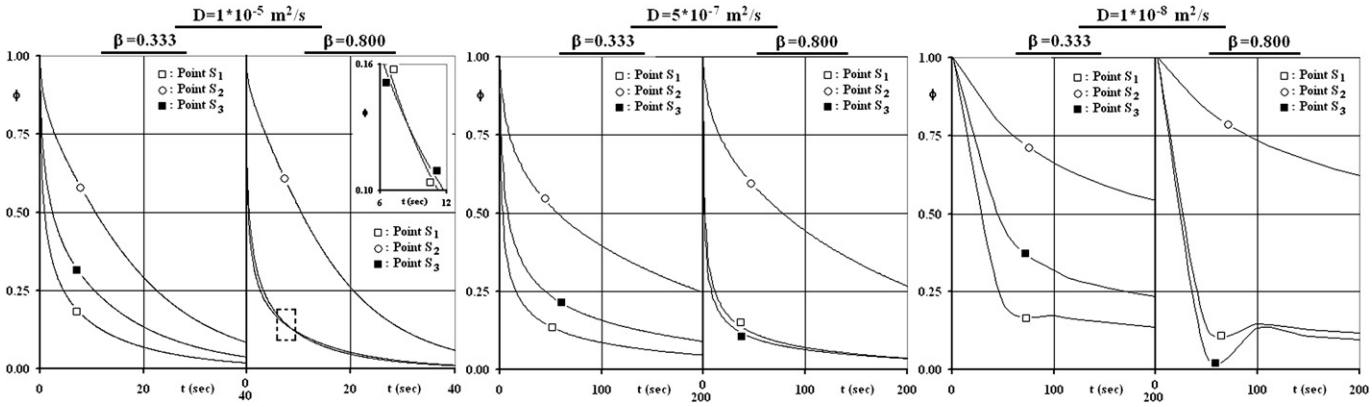

Fig. 9. Drying characteristics at the cylinder surface locations of S_1, S_2 and S_3 for the moisture diffusivity and blockage ratio cases of $D = 1 \times 10^{-5}$ and 5×10^{-7} and 1×10^{-8} m^2/s and $\beta = 0.333 \times 0.800$.

the state of the surface moisture layout, in the lowest blockage case of $\beta = 0.333$, comes out to be sequenced as $\phi_{S_2} > \phi_{S_3} > \phi_{S_1}$, in the lowest blockage case of $\beta = 0.800$ the order of the moisture contents at S_1 and S_3 replaces resulting in $\phi_{S_2} > \phi_{S_1} > \phi_{S_3}$. This finding puts forward the fact that surface moisture levels are characterized significantly by h_m and secondarily by D. It can additionally be noticed from the figure that in lower moisture diffusivity and higher blockage ratio cases, back-face moisture levels (ϕ_{S_2}) deviate more remarkably from the front (ϕ_{S_1}) and throat (ϕ_{S_3}) values. Moreover, Fig. 9 further identifies that ϕ_{S_1} and ϕ_{S_3} of the drying scenario with $\beta = 0.333$ are higher than those of $\beta = 0.800$, where the contrary is valid for the ϕ_{S_2} values. These 2 issues can be associated by the variation of surface mass transfer coefficient distributions shown in Fig. 5. These records not only completely match the iso-moisture contours of Fig. 8, but they are also essential for the industrial processes, where forced-drying need to be focused to specific surface coordinates of cylindrical bodies, which can be supervised by the blockage effect.

It is also aimed not only to verify the numerical accuracy of the developed ADI based software but also to validate its relevancy to real time industrial drying applications. The extra computation, based on the experimental scenario components of $U_\infty = 0.33$ m/s, $T_\infty = 39.9$ °C, $h_m = 1.66 \times 10^{-7}$ m/s, $M_i = 3.43$ kg/kg, $D = 4.59 \times 10^{-10}$ m^2/s, as applied by Queiroz and Nebra [19] for banana drying, sufficiently clarifies the trustable character of the developed software (Fig. 10).

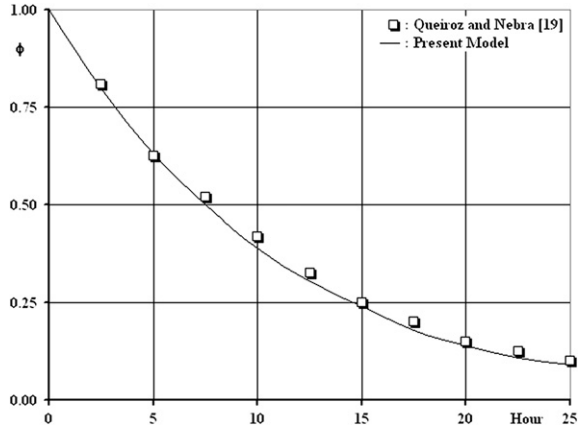

Fig. 10. Experimental and computed dimensionless moisture content distributions.

4. Conclusions

In this paper, the effects of confined flow on the hydrodynamic, thermal and mass transfer characteristics of a circular cylinder and the interrelation of these mechanisms are investigated numerically. Some essential points and findings of the present work are given as follows:

- The computed recirculation lengths of $L_r = \sim 47.3$ mm, ~ 26.9 mm and ~ 16.7 mm for $\beta = 0.333$, 0.571 and 0.800 indicate that the influence and strength of the downstream vortex system becomes weaker at high blockage cases.
- The maximum wall shear stress locations are evaluated to shift downstream with higher blockage.
- The minimum surface static pressure locations of $\theta_{P_s-\min} = 93.5^\circ \rightarrow 109.9^\circ$ ($\beta = 0.333 \rightarrow 0.800$) not only designate their placement in between the throat and separation points but also their shift to further angular positions in high β cases.
- The augmenting role of blockage on the heat transfer rates is identified with the interpreting figures of $Nu_{ave} = 4.05$, 4.97 and 6.51 for $\beta = 0.333$, 0.571 and 0.800.
- The magnitude of blockage effect on heat transfer rates is evaluated to differ at different angular positions on the cylinder surface. As the $h_{\beta=0.800}/h_{\beta=0.333}$ and $h_{\beta=0.571}/h_{\beta=0.333}$ ratios are computed as 1.19 and 1.11 at the stagnation point ($\theta = 0^\circ$), they promote to 2.51 and 1.42 at the throat ($\theta = 90^\circ$), which identifies the significance of boundary layer thinning on the heat transfer mechanism.
- Moisture diffusivity is determined to have more impact on overall drying times at higher blockage cases.
- The augmenting influence of blockage on the mass transfer mechanism at higher moisture diffusivity is exposed by the characteristic ratios of $\Delta t_{od-\beta=0.333}/\Delta t_{od-\beta=0.800} = 1.032-1.199$ for $D = 1 \times 10^{-8}$ m^2/s and 1×10^{-5} m^2/s.
- As center and average moisture levels are computed to differ significantly at the beginning of the drying process, the gap among them is evaluated to be only 1.6% in the last 5% of the drying period.
- Surface mass transfer coefficients come out to be quite determinative on the front and back face moisture levels in cases with high moisture diffusivity ($D = 1 \times 10^{-5}$ m^2/s); however in drying applications with lower diffusivity ($D = 1 \times 10^{-8}$ m^2/s), almost symmetric moisture distributions within the cylinders are evaluated, indicating similar front and back face moisture levels.

References

[1] A.M. Al-Amiri, K.M. Khanafer, Numerical simulation of double-diffusive mixed convection within a rotating horizontal annulus. International Journal of Thermal Sciences 45 (2006) 567–578.

[2] C.A. Chaves, J.R. Camargo, S. Cardoso, Transient natural convection heat transfer by double diffusion from a heated cylinder buried in a saturated porous medium. International Journal of Thermal Sciences 44 (2005) 720–725.

[3] L.L. Vasiliev, L.E. Kanonchik, A.G. Kulakov, Hydrogen storage system based on novel carbon materials and heat pipe heat exchanger. International Journal of Thermal Sciences 46 (2007) 914–925.

[4] I. Dincer, A.Z. Sahin, A new model for thermodynamic analysis of a drying process. International Journal of Heat and Mass Transfer 47 (2004) 645–652.

[5] J. Chakraborty, N. Verma, R.P. Chhabra, Wall effects in flow past a circular cylinder in a plane channel: a numerical study. Chemical Engineering and Processing 43 (2004) 1529–1537.

[6] M.D. Griffith, M.C. Thompson, T. Leweke, K. Hourigan, W.P. Anderson, Wake behaviour and instability of flow through a partially blocked channel. Journal of Fluid Mechanics 582 (2007) 319–340.

[7] S. Sen, S. Mittal, G. Biswas, Steady separated flow past a circular cylinder at low Reynolds numbers. Journal of Fluid Mechanics 620 (2009) 89–119.

[8] F. Rehimi, F. Aloui, S. Ben Nasrallah, Experimental investigation of a confined flow downstream of a circular cylinder centered between two parallel walls. Journal of Fluids and Structures 24 (2008) 855–882.

[9] M. Sahin, R.G. Owens, A numerical investigations of wall effects up to high blockage ratios on two-dimensional flow past a confined circular cylinder. Physics of Fluids 16 (2004) 1305–1320.

[10] S. Camarri, F. Giannetti, On the inversion of the von Karman street in the wake of a confined square cylinder. Journal of Fluid Mechanics 574 (2007) 169–178.

[11] M. Breuer, J. Bernsdorf, T. Zeiser, F. Durst, Accurate computations of the laminar flow past a square cylinder based on two different methods: lattice-Boltzmann and finite-volume. International Journal of Heat and Fluid Flow 21 (2000) 186–196.

[12] R.P. Bharti, R.P. Chhabra, V. Eswaran, Effect of blockage on heat transfer from a cylinder to power law liquids. Chemical Engineering Science 62 (2007) 4729–4741.

[13] B.H. Chang, A.F. Mills, Effect of aspect ratio on forced convection heat transfer from cylinders. International Journal of Heat and Mass Transfer 47 (2004) 1289–1296.

[14] W.A. Khan, J.R. Culham, M.M. Yovanovich, Fluid flow around and heat transfer from an infinite circular cylinder. Journal of Heat Transfer 127 (2005) 785–790.

[15] E. Buyruk, M.W. Johnson, I. Owen, Numerical and experimental study of flow and heat transfer around a tube in cross-flow at low Reynolds number. International Journal of Heat and Fluid Flow 19 (1998) 223–232.

[16] W.A. Khan, J.R. Culham, M.M. Yovanovich, Fluid flow and heat transfer from a cylinder between parallel planes. Journal of Thermophysics and Heat Transfer 18 (2004) 395–403.

[17] A.K. Dhiman, R.P. Chhabra, V. Eswaran, Flow and heat transfer across a confined square cylinder in the steady flow regime: rffect of Peclet number. International Journal of Heat and Mass Transfer 48 (2005) 4598–4614.

[18] A. Sharma, V. Eswaran, Effect of channel confinement on the two-dimensional laminar flow and heat transfer across a square cylinder. Numerical Heat Transfer, Part A: Applications 47 (2004) 79–107.

[19] M.R. Queiroz, S.A. Nebra, Theoretical and experimental analysis of the drying kinetics of bananas. Journal of Food Engineering 47 (2001) 127–132.

[20] E.K. Akpinar, I. Dincer, Application of moisture transfer models to solids drying. Proceedings of the Institution of Mechanical Engineers Part A 219 (2005) 235–244.

[21] P.G. Ganesan, P.H. Rani, Unsteady free convection MHD flow past a vertical cylinder with heat and mass transfer. International Journal of Thermal Sciences 39 (2000) 265–272.

[22] A. Kaya, O. Aydin, I. Dincer, Numerical modeling of forced convection drying of cylindrical moist objects. Numerical Heat Transfer, Part A: Applications 51 (2007) 843–854.

[23] M.M. Hussain, I. Dincer, Two-dimensional heat and moisture transfer analysis of a cylindrical moist object subjected to drying: a finite-difference approach. International Journal of Heat and Mass Transfer 46 (2003) 4033–4039.

[24] A. Kondjoyan, A review on surface heat and mass transfer coefficients during air chilling and storage of food products. International Journal of Refrigeration 29 (2006) 863–875.

[25] I. Dincer, M.M. Hussain, B.S. Yilbas, A.Z. Sahin, Development of a new drying correlation for practical applications. International Journal of Energy Research 26 (2002) 245–251.

[26] A.Z. Sahin, I. Dincer, Graphical determination of drying process and moisture transfer parameters for solids drying. International Journal of Heat and Mass Transfer 45 (2002) 3267–3273.

[27] N.M. Panagiotou, M.K. Krokida, Z.B. Maroulis, G.D. Saravacos, Moisture diffusivity: literature data compilation for foodstuffs. International Journal of Food Properties 7 (2004) 273–299.

[28] M.A. Teamah, Numerical simulation of double diffusive laminar mixed convection in a horizontal annulus with hot, solutal and rotating inner cylinder. International Journal of Thermal Sciences 46 (2007) 637–648.

[29] W.A.M. McMinn, T.R.A. Magee, Air drying kinetics of potato cylinders. Drying Technology 14 (1996) 2025–2040.

[30] F.P. Incropera, D.P. DeWitt, Fundamentals of Heat and Mass Transfer. John Wiley and Sons, New York, 2001.

[31] Ansys Cfx, User Manual, 2005.

[32] A. Kaya, O. Aydin, I. Dincer, Numerical modeling of heat and mass transfer during forced convection drying of rectangular moist objects. International Journal of Heat and Mass Transfer 49 (2006) 3094–3103.

[33] H. Feng, J. Tang, J. Dixon-Warren, Determination of moisture diffusivity of red delicious apple tissues by thermogravimetric analysis. Drying Technology 18 (2000) 1183–1199.

[34] S. Simal, C. Rossell, A. Berna, A. Mulet, Drying of shrinking cylinder-shaped bodies. Journal of Food Engineering 37 (1998) 423–435.

[35] M.K. Krokida, E. Foundoukidis, Z. Maroulis, Drying constant: literature data compilation for foodstuffs. Journal of Food Engineering 61 (2004) 321–330.

[36] M. Kawaguti, P. Jain, Numerical study of a viscous fluid flow past a circular cylinder. Journal of Physics Society of Japan 61 (1966) 1998–2055.

[37] G. Biswas, S. Sarkar, Effect of thermal buoyancy on vortex shedding past a circular cylinder in cross-flow at low Reynolds numbers. International Journal of Heat and Mass Transfer 52 (2009) 1897–1912.

[38] H. Takami, H.B. Keller, Steady two-dimensional viscous flow of an incompressible fluid past a circular cylinder. Physics of Fluids (1969) 51–56.

[39] S.C.R. Dennis, G.-Z. Chang, Numerical solutions for steady flow past a circular cylinder at Reynolds numbers up to 100. Journal of Fluid Mechanics 42 (1970) 471–489.

[40] M.H. Wu, C.Y. Wen, R.H. Yen, Experimental and numerical study of the separation angle for flow around a circular cylinder at low Reynolds number. Journal of Fluid Mechanics 515 (2004) 233–260.

[41] W. Schonauer, Ein differenzenverfahren zur lösung der grenzschichtgleichung für stationäre, laminare, inkompressible strömung. Ing.-Arch. 33 (1964) 173.

[42] A. Zukauskas, J. Ziugzda, Heat Transfer of a Cylinder in Crossflow. Hemisphere, New York, 1985.

[43] S.C.R. Dennis, J.D. Hudson, N. Smith, Steady laminar forced convection from a circular cylinder at low Reynolds number. Physics of Fluids 11 (1968) 933–940.

[44] H. Jafroudi, H.T. Yang, Steady laminar forced convection from a circular cylinder. Journal of Computational Physics 65 (1986) 45–56.

[45] C.J. Apelt, M.A. Ledwich, Heat transfer in transient and unsteady flows past a circular cylinder in the range $1 < R < 40$. Journal of Fluid Mechanics 95 (1979) 761–777.

[46] A.A. Ozalp, 1st and 2nd law characteristics in a micropipe: integrated effects of surface roughness, heat flux and Reynolds number. Heat Transfer Engineering 30 (2009) 973–987.

[47] H. Umur, A.A. Ozalp, Fluid flow and heat transfer in transitional boundary layers: effects of surface curvature and free stream velocity. Heat and Mass Transfer 43 (2006) 7–15.

[48] A.B. Turner, S.E. Hubbe-Walker, F.J. Bayley, Fluid flow and heat transfer over straight and curved rough surfaces. International Journal of Heat and Mass Transfer 43 (2000) 251–262.

[49] N.T. Obot, Toward a better understanding of friction and heat/mass transfer in microchannels—a literature review. Microscale Thermophysics Engineering 6 (2002) 155–173.